ARL-TR-8417 ●JULY 2018

US Army Research Laboratory

Flash Sintering of Li-Ion Conducting Lithium Lanthanum Titanate for Li–Air Batteries

by Victoria L Blair, Selva Vennila Raju, Aubrey L Fry, Michael Kornecki, Jeffrey Wolfenstine, and Raymond E Brennan

NOTICES

Disclaimers

The findings in this report are not to be construed as an official Department of the Army position unless so designated by other authorized documents.

Citation of manufacturer's or trade names does not constitute an official endorsement or approval of the use thereof.

Destroy this report when it is no longer needed. Do not return it to the originator.

ARL-TR-8417 ● JULY 2018

US Army Research Laboratory

Flash Sintering of Li-Ion Conducting Lithium Lanthanum Titanate for Li–Air Batteries

by Victoria L Blair and Raymond E Brennan
Weapons and Materials Research Directorate, ARL

Jeffrey Wolfenstine
Sensors and Electron Devices Directorate, ARL

Selva Vennila Raju
Oak Ridge Associated Universities

Aubrey L Fry
Oak Ridge Institute for Science and Education

Michael Kornecki
SURVICE Engineering

REPORT DOCUMENTATION PAGE

Form Approved
OMB No. 0704-0188

1. REPORT DATE *(DD-MM-YYYY)*	2. REPORT TYPE	3. DATES COVERED (From - To)
July 2018	Technical Report	October 2017–February 2018

4. TITLE AND SUBTITLE
Flash Sintering of Li-Ion Conducting Lithium Lanthanum Titanate for Li–Air Batteries

5a. CONTRACT NUMBER
W911QX-16-D-0014 / 1120-1120-99

5b. GRANT NUMBER

5c. PROGRAM ELEMENT NUMBER

6. AUTHOR(S)
Victoria L Blair, Selva Vennila Raju, Aubrey Fry, Michael Kornecki, Jeffrey Wolfenstine, and Raymond E Brennan

5d. PROJECT NUMBER

5e. TASK NUMBER

5f. WORK UNIT NUMBER

7. PERFORMING ORGANIZATION NAME(S) AND ADDRESS(ES)
US Army Research Laboratory
Weapons and Materials Research Directorate (ATTN: RDRL-WMM-E)
Aberdeen Proving Ground, MD 21005

8. PERFORMING ORGANIZATION REPORT NUMBER
ARL-TR-8417

9. SPONSORING/MONITORING AGENCY NAME(S) AND ADDRESS(ES)

10. SPONSOR/MONITOR'S ACRONYM(S)
MMSD

11. SPONSOR/MONITOR'S REPORT NUMBER(S)

12. DISTRIBUTION/AVAILABILITY STATEMENT
Approved for public release; distribution is unlimited.

13. SUPPLEMENTARY NOTES

14. ABSTRACT
The US Army needs high energy density, lightweight batteries, which can reduce Soldier load by up to 14 lb. One potential method to reduce the load is to replace disposable, alkaline batteries with lithium (Li)–air batteries, which weigh less due to high energy density and a porous “air” cathode. Li–air battery performance is limited by the electrolytic membrane, which must have an extremely high Li-ion conductivity. $Li_{0.33}La_{0.55}TiO_3$ (LLTO) is a promising electrolytic membrane material due to its high lattice conductivity; however, the total conductivity of LLTO is lowered by its grain-boundary properties. Previous work shows careful structural modification and processing can improve the grain-boundary conductivity. For the current work, flash sintering densifies LLTO at temperatures well below the conventional sintering temperature. Excessive volatilization of Li could be avoided by reducing the time of exposure to high temperatures to improve grain-boundary conductivity. X-ray diffraction of the flashed specimens showed no significant phase change among specimens processed by other methods. Electrochemical-impedance-spectroscopy measurements were taken and results modelled to understand the nature of conductivity within the flashed samples. The effects of flash sintering on the microstructure and conductivity in comparison with conventionally sintered samples are discussed.

15. SUBJECT TERMS
LLTO, $Li_{0.33}La_{0.55}TiO_3$, flash sintering, lithium volatilization, ionic conductivity, battery materials

16. SECURITY CLASSIFICATION OF:			17. LIMITATION OF ABSTRACT	18. NUMBER OF PAGES	19a. NAME OF RESPONSIBLE PERSON
a. REPORT	b. ABSTRACT	c. THIS PAGE			Victoria L Blair
Unclassified	Unclassified	Unclassified	UU	29	19b. TELEPHONE NUMBER (Include area code) 4103064947

Contents

List of Figures

List of Tables

Acknowledgments

This work was presented at the 2018 Conference on Electronic and Advanced Materials on 18 January 2018 in the Electromagnetic Field Effects on Ceramic Processing Symposium.

This work benefited from ionic-conductivity measurements performed at the University of Michigan, courtesy of Dr Jeff Sakamoto and his student Michael Wang.

SV Raju was sponsored by the US Army Research Laboratory (ARL) under Cooperative Agreement No. W911NF-16-2-0050. The views and conclusions contained in this document are those of the authors and should not be interpreted as representing the official policies, either expressed or implied, of ARL or the US Government. The US Government is authorized to reproduce and distribute reprints for Government purposes notwithstanding any copyright notation herein.

AL Fry was supported in part by an appointment to the Postgraduate Research Participation Program at ARL administered by the Oak Ridge Institute for Science and Education through an interagency agreement between the US Department of Energy and ARL.

The research reported in this document was performed in connection with contract/instrument W911QX-16-D-0014 with the ARL. The views and conclusions contained in this document are those of SURVICE Engineering and ARL. Citation of manufacturer's or trade names does not constitute an official endorsement or approval of the use thereof. The US Government is authorized to reproduce and distribute reprints for Government purposes notwithstanding any copyright notation hereon.

1. Introduction

Lithium (Li)-ion batteries are currently one of the leading energy-storage-device technologies, and the US Army is interested in continuing to develop novel battery materials to aid the warfighter. The technologies employed by Soldiers (radios, surveillance equipment, etc.) require portable energy supplies, and current lithium ion batteries can only supply 6–8 h of continuous power before needing to be replaced or charged. If novel battery devices were developed and implemented, potential benefits for extending the supply energy beyond 72 h and expanding to multiple devices could be possible. Additionally, the number and total weight of batteries could be reduced if the energy density was higher, leading to lower risk of musculoskeletal injuries sustained by the Soldier. Li–air batteries have been the focus of recent research, as they can supply up to 10× higher energy due to the porous "air" cathode, which reduces the weight of the device.[1]

Both low electrical conductivity and high Li-ion conductivity are required for efficient battery operation, while the chemical stability and mechanical robustness are necessary to support the reliability and safety of the battery, respectively. One of the most promising candidates for this membrane material is lithium lanthanum titanate, $Li_{3x}La_{(2/3)-x}TiO_3$ (LLTO), due to its high theoretical lattice conductivity.[2] This study will focus on LLTO with x = 0.11 ($Li_{0.33}La_{0.55}TiO_3$), as previous work indicates LLTO ceramics with this composition exhibit the maximum lattice conductivity.[3,4]

1.1 Methods to Improve Conductivity in LLTO

The low total conductivity observed in LLTO ceramic materials is believed to arise from three main factors: lithium deficiency, low density, and high resistivity at the grain boundaries. All three of those factors influence each other; for example, sintering at higher temperatures may increase the density (thus increasing conductivity) but may also lead to Li loss through volatilization of Li_2O and simultaneously decrease conductivity due to loss of the main charge carriers.[2]

Recently, there has been significant effort toward improving the grain-boundary conductivity in LLTO and related ceramic-membrane materials. One method for increasing the grain-boundary conductivity is to maximize the density of the part such that it approaches the theoretical density (TD), as explored by Weiss Brennan et al.[5] Density optimization is expected to enhance grain-boundary conductivity, since recent transmission-electron-microscopy results on LLTO indicate the majority of porosity exists at the grain boundaries.[6]

Increasing the surface area at the grain boundaries by improving the density should enhance the Li-ion diffusion pathways at the grain boundaries. Minimization of the detrimental grain-boundary second phase (i.e., air) should increase the total conductivity as well.[3,6] These ideas were partially investigated by Weiss Brennan et al.[5] Additionally, US Army Research Laboratory (ARL) researchers studied the effects of hot isostatic pressing (HIP) of LLTO and found the material could remain in the cubic phase at near TD. In this case, however, the conductivity of the material was similar to that of a non-HIPed part.[7] It was possible the extended period of time at the sintering temperature led to significant volatilization of Li. This type of loss could lead to a lower concentration of charge carriers, reducing the ionic conductivity of the material. ARL researchers have also concluded that a combination of grain-boundary engineering, high density, and maintenance of the concentration of the charge carriers could also improve the grain-boundary conductivity by a factor of three.[8]

LLTO, a perovskite, comes in two different polymorphs: tetragonal ($P4/mmm$) or cubic ($Pm\overline{3}m$). The tetragonal structure is stabilized upon slow cooling from a sintering temperature of 1200 °C. If a rapid-cooling regime is used, such as quenching into liquid nitrogen, the cubic phase ($Pm\overline{3}m$) is stabilized.[9–12] Harada et al. determined that LLTO tends to crystallize with a ratio of both phases, depending on the cooling schedule and the A-site composition.[9] Additionally, Harada showed that the lattice conductivities (σ_l) for the tetragonal phase was 60% lower than that of the cubic phase. The change in lattice conductivity from one phase to the next may have been due to the symmetry of the cubic space group. In the cubic phase, the angle between the octahedra (as shown in Fig. 1) was slightly larger than the angle in the tetragonal phase. This tilting of the octahedra may have resulted in a lower activation energy for Li-ion conduction through the cubic lattice, leading to a higher lattice conductivity.[9–12]

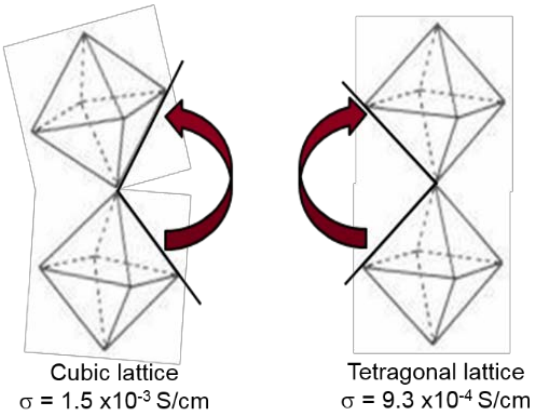

Fig. 1 Idealized cubic lattice (left) shows tilting of the octahedral causing a larger space for Li-ion conduction in comparison to the idealized tetragonal structure (right)

1.2 Flash Sintering

Flash sintering is a relatively new technique gaining traction in the ceramic-sintering community due to its ability to rapidly sinter materials at significantly lower furnace temperatures than conventional sintering methods. The technique was first examined by Cologna et al. in 2011, demonstrating sintering of yttria stabilized zirconia (YSZ) in a matter of seconds by applying an electric field across the sample and ramping the furnace to 750 °C.[13] Since its discovery, the academic and research communities have expanded the research to include understanding the fundamental mechanisms that enable densification of these high melting-temperature (T_m) materials in a short period of time.

The flash-sintering process has been described as a dynamic one in which a green ceramic part sinters quickly due to a transition in electrical conductivity, leading to joule heating within the part. This joule heating enables the part to reach the sintering temperature very quickly. Typically, the DC power supply switches from voltage-driven to current-driven to prevent electrical runaway, which could damage the power supply. As the material sinters, the electrical resistance decreases and eventually reaches steady state once densification is complete. However, this occurs in a matter of seconds.[14] Much of the early research on this phenomena was explored by Raj et al. at the University of Colorado at Boulder.[14] The mechanism of flash sintering is still under academic debate, and the materials to which flash sintering can be applied are still being examined.[13–19]

1.3 Motivation and Research Objective

This ongoing work will examine the effectiveness of flash sintering, as opposed to conventional pressureless sintering, when applied to LLTO. As described earlier, the crystal structure of LLTO is extremely sensitive to heating and cooling rates, which can affect grain conductivity. The lower furnace temperatures and shorter times could greatly reduce the amount of lithium volatilization and also influence the final conductivity. Therefore, it is hypothesized that flash sintering will lead to dense LLTO materials with ionic conductivity rivalling conventionally sintered samples due to the high heating rates and short exposure times to high temperatures.

2. Experimental Procedure

2.1 Materials Processing

LLTO powder was synthesized by the same method described by Weiss Brennan et al.,[5] in which reagent-grade oxides and carbonates were mixed together and

calcined at 1100 °C in air for 1 h. The prereacted LLTO powder was then consolidated into green parts by making a slurry from the calcined powder and pouring it into a plastic mold to produce approximately 3- × 3- × 12-mm rectangular bars. All results from the conventionally sintered specimens were derived from previous ARL technical reports.[5,7,8]

By using two different sample geometries, the application of voltage and the resulting voltage per area could be altered. Figure 2 shows the experimental setup in parallel-plate configuration, in which a bar or disk is placed between two metallic electrodes connected to the power supply.

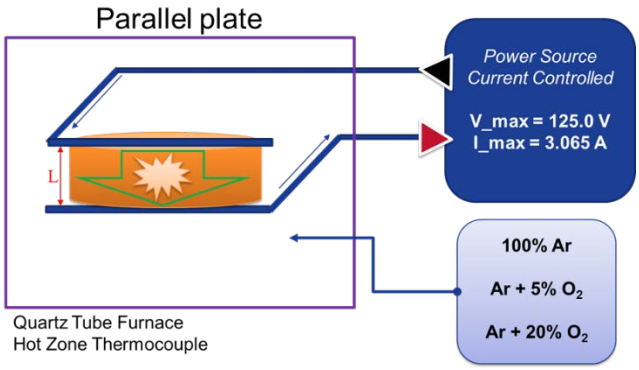

Fig. 2 Experimental schematic of the tube furnace (purple box), electrical leads and electrodes (blue lines), and sample (orange): setup uses pressed disks between two metal plates as electrodes that are connected to wires going to the power supply; atmosphere in the furnace can be adjusted (e.g., argon [Ar] or Ar–oxygen [O_2] mixes)

Figure 3 shows the experimental setup for a slip-cast rectangular bar, which can be placed directly on top of the nickel–chromium-alloy (nichrome) wire electrodes that connect to the power supply. In this case, the sample length is greater than that of a pressed disk but the overall sample volume is smaller, which could lead to a larger power density.

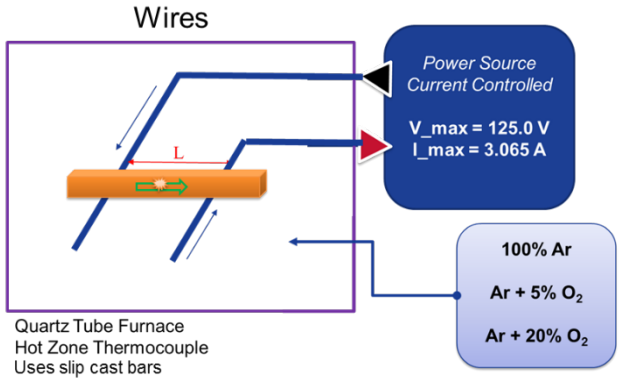

Fig. 3 Experimental schematic of the tube furnace (purple box), electrical leads (blue lines), and sample (orange): setup uses slip-cast bars laid on two metal wires that go to the power supply; furnace can be back-filled with gases such as Ar and Ar–O_2 mixes

The experiments were documented by tracking the voltage drop across the sample during ramping of the furnace temperature. The furnace temperature at which the voltage suddenly dropped was defined as the flash temperature. The flash event was accompanied by a bright orange or yellow emission from the sample, in contrast to the dull-red background color in the furnace. Table 1 lists experiment configurations from four flash sintering cycles.

Table 1 Parameters of the experiments described in this report

Experiment	Configuration	$V_{applied}$ (volts)	Furnace gas	Flash temperature (°C)
1	W parallel plate (bar)	125	Ar	N/A
2	Nichrome wires (bar)	125	Ar	768
3	Pt Parallel plate (bar)	60	Ar	636
4	Pt Parallel plate (disk)	75	5.18% O_2–Ar	1000

Note: W = tungsten; Pt = platinum.

2.2 Characterization of Parts

In order to complete work with a scanning electron microscope (SEM), the samples were freshly fractured and set onto sticky carbon tape. Fresh fracture of the specimens was completed to reduce any potential contamination of the sample during handling. They were then imaged using a Hitachi S-4700 SEM. A small fragment of sample was crushed in an agate mortar and pestle, mixed with alcohol, and dripped onto silicon zero-background sample holders to determine the phase content via powder X-ray diffraction (XRD). Specimens from previous research (described in a 2016 ARL technical report[8]) were also crushed and measured with a Bruker D2 Phaser to obtain data for Rietveld-refinement calculation of the phases. The data were imported into TOPAS software (Bruker AXS, Inc.) and modeled assuming both the cubic ($Pm\overline{3}m$) and tetragonal ($P4/mmm$) structures were present.

Specimens from Experiments 3 and 4 were measured by electrochemical impedance spectroscopy (EIS) to calculate the ionic conductivity of the grains and grain boundaries. The specimens were gently polished using water and diamond-impregnated films and shaped into parallelepipeds, which were coated with 30-nm-thick gold electrode. The conductivity was measured from 0.1 Hz to 1 MHz with a potential amplitude of 100 mV. Figure 4 shows idealized data expected from either an ionic conducting material (expected result for LLTO) or an electronic conducting material (expected result for a metal such as copper).

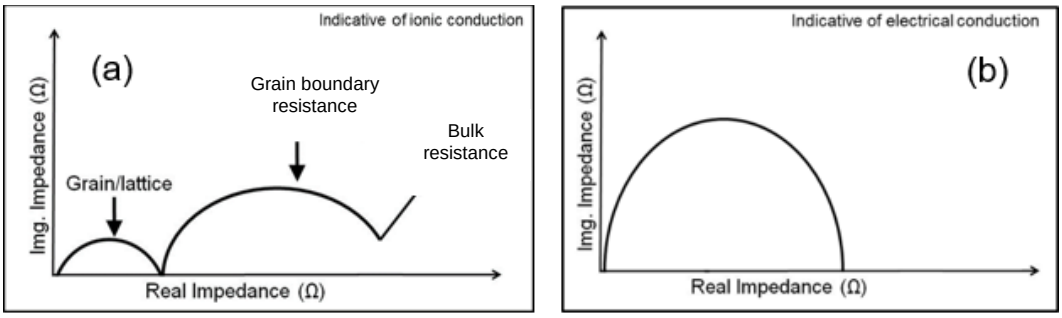

Fig. 4 Example of a) EIS data from an ionic conducting material and b) an electrical conducting material

These data were fit to an equivalent circuit to provide the bulk resistance (R_b), grain-boundary resistance (R_{gb}), and capacitance. The values were then plugged into the conductivity equations (Eqs. 1 and 2) along with the specimen dimensions to obtain the conductivity of either the bulk (σ_b) or the grain boundaries (σ_{gb}), where l is the specimen length and A is the cross-sectional area.

$$\sigma_b = \frac{l}{R_b A} \tag{1}$$

and

$$\sigma_{gb} = \frac{l}{R_{gb} A}. \tag{2}$$

3. Results

3.1 Microstructure and the Flash Event

Experiment 1 was the first attempt at flash-sintering LLTO. The sample was a rectangular fragment (bar shaped) from a uniaxially pressed and cold isostatically pressed "dog bone" specimen (description of dog-bone die included in Cologna et al.[13]); the bar was placed between parallel-plate W electrodes. The bar had starting dimensions (length × width × height) of 12.5 mm × 3.7 mm × 1.6 mm. The furnace was heated at 10 °C/min up to 1000 °C under flowing Ar. The sample flashed as the power supply was discharged in current-control mode. The data logger malfunctioned and did not collect any voltage data during the experiment.

Figure 5 shows an SEM image from the fracture surface of a specimen from Experiment 1. An apparent density gradient was observed from the edge closest to the W electrode (Region 1) through the thickness to the green compact-like microstructure (Region 3), following the arrow in green.

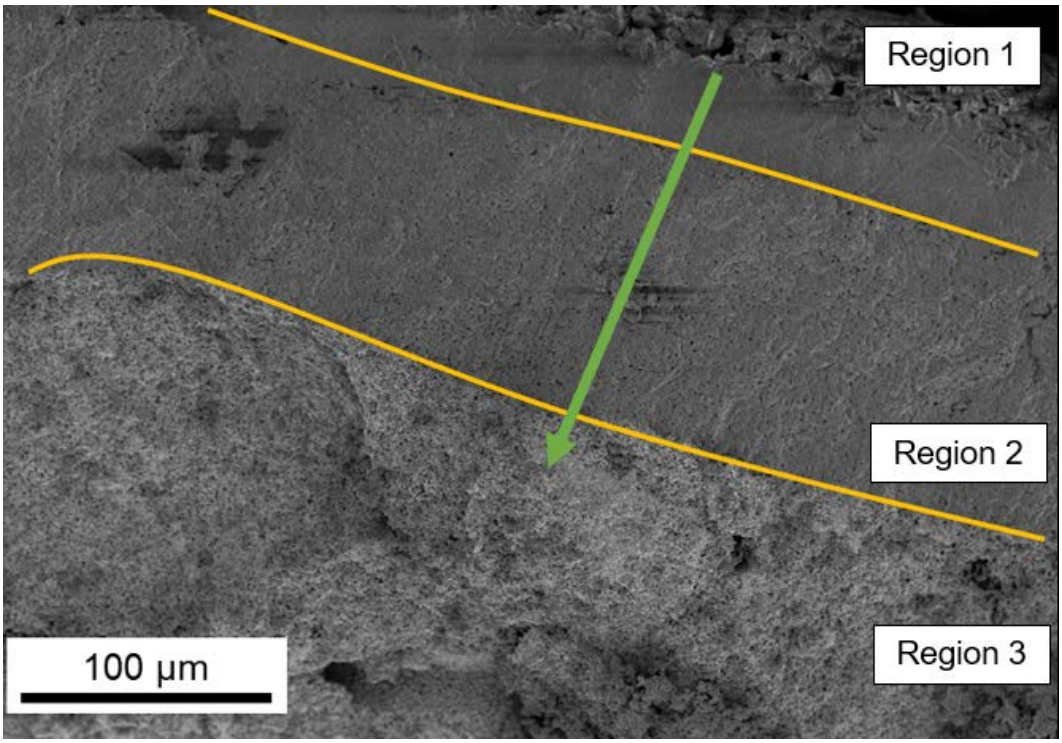

Fig. 5 SEM image of specimen from Experiment 1 taken on edge near W electrode (100-micron scale bar): yellow lines represent approximate areas where microstructure changes were observed; Region 1 is densest with limited porosity, Region 2 has more porosity, and Region 3 is essentially a green compact; green line indicates direction of decreasing density

Figure 6 shows the SEM images from Regions 1 and 2 of Experiment 1. While both regions exhibit porosity, Region 2 appears to have significantly more than Region 1. The grains in Region 2 appear to have formed necks and exhibit partial densification, as there is limited interconnectivity in the remaining porosity.

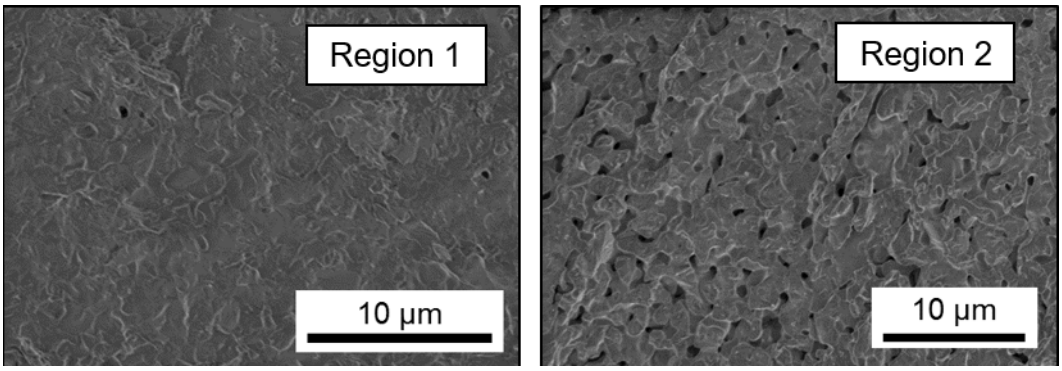

Fig. 6 SEM images of Region 1 (left) and Region 2 (right) from Experiment 1

The sample underwent 11% volumetric shrinkage (by measuring the geometry before and after flash) during the flash experiment. However, considering these

parts had a green density that was approximately 45% of the TD, to get to a final density of 95% of TD the parts should shrink by approximately 50%. This indicates that 11% volumetric shrinkage on this part would lead to a density that is approximately 56% of the TD.

Experiment 2 was conducted in a similar manner to Experiment 1, but with a different geometry. The sample was a slip-cast bar of geometry 12.5 mm × 3.9 mm × 3.1 mm laid onto two nichrome wires. Figure 7 shows the furnace temperature and sample voltage versus time in minutes. From these data, the flash temperature (T_f) was estimated as 768 °C, which was significantly lower than the conventional sintering temperature of 1200 °C. After the initial voltage drop, the furnace was held at the flash temperature for 5 min with the current applied.

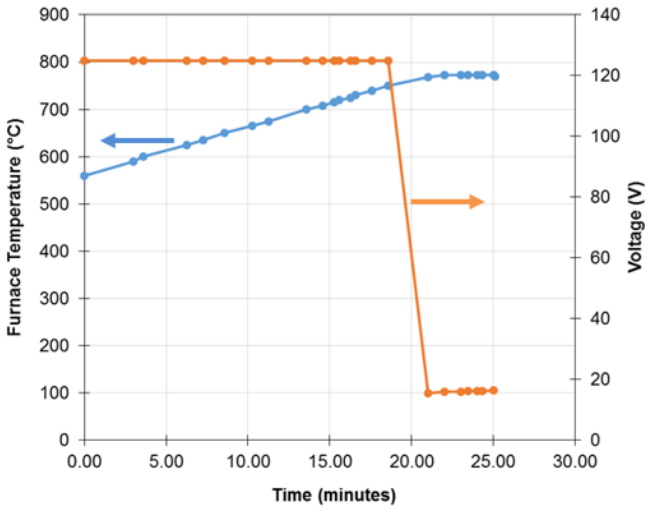

Fig. 7 Graph shows furnace temperature and sample voltage vs. time in minutes (data were recorded manually and do not indicate full furnace cycle); flash onset occurs at ~ 18 min as indicated by voltage drop

Figure 8 shows an SEM image of the specimen from Experiment 2. The grain size of this specimen appeared to be smaller than the grain sizes from Experiment 1. This was likely due to the amount of time the sample was at high temperature. One of the drawbacks to the experimental set-up was the sample temperature could not be accurately measured during the flash event, making it difficult to assess the heating rate or how long the sample was at the densification temperature.

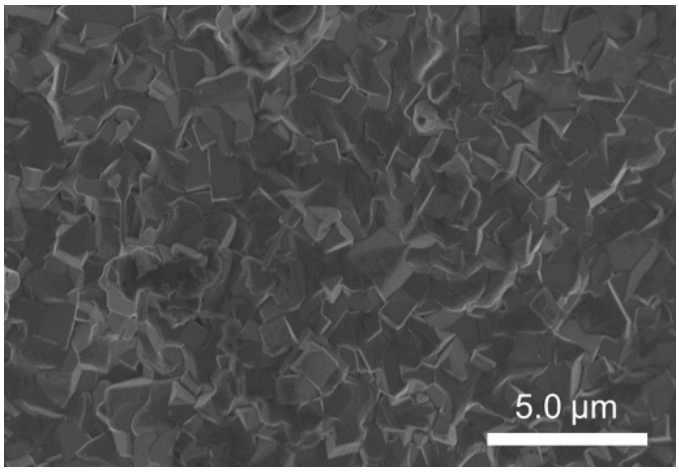

Fig. 8 SEM image of the specimen from Experiment 2 (5-micron scale bar)

Another observation from Experiment 2 was that the nichrome wires were melted at the point where the sample made contact. Nichrome wire has a T_m of 1400 °C; therefore, it is possible the maximum temperature of the sample was approximately 1400 °C. Despite the high sample temperature, which should have led to significant densification, the short exposure time resulted in a final grain size of approximately 1 micron.

Experiment 3 was also run on a rectangular bar of size 11 mm × 3.5 mm × 2.5 mm, but when the sample was pressed between the metallic electrode plates it broke in half. While the experiment was continued the two pieces of the sample remained separated by an air gap, effectively creating two specimens. One specimen was imaged in the SEM while the other was used for XRD analysis. This experiment used Pt-plate electrodes as opposed to W, since they had a higher melting temperature and were less reactive than W. The distance between the electrodes (length "L" in Fig. 3) was the same for both specimens in Experiment 3. Figure 9 shows the furnace temperature and voltage versus time, with the flash temperature estimated as 636 °C. Once the initial voltage dropped, the furnace was held at the flash temperature for 5 min with the current applied.

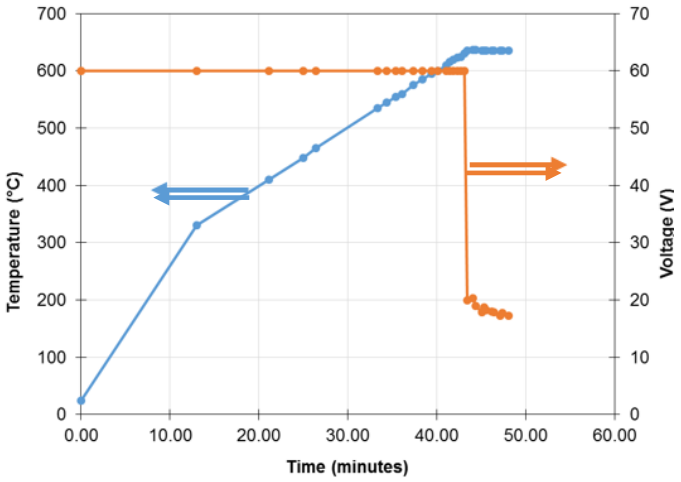

Fig. 9 Furnace temperature and sample voltage vs. time for Experiment 3

Figure 10 shows an SEM image of the specimen from Experiment 3. Region 1 indicates the surface of the specimen that was in contact with the Pt electrode, while Region 2 is a fracture surface in which a chip of material broke off during sample handling after the flash event.

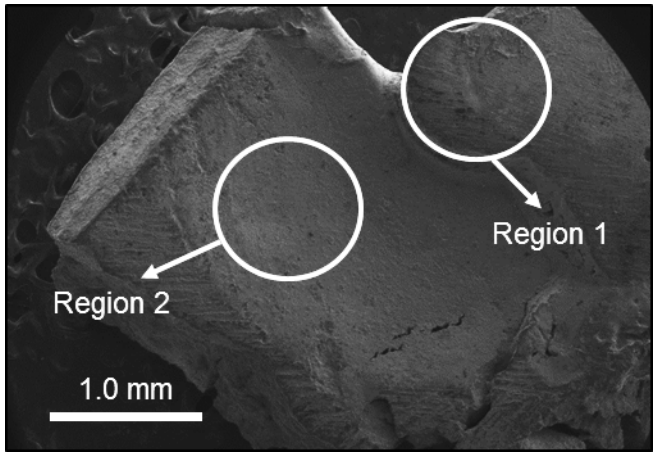

Fig. 10 SEM image of Experiment 3's specimen, whose Region 1 is the surface that was against the electrode while Region 2 is a fracture surface (1-mm scale bar)

Figure 11 shows Regions 1 and 2 at higher magnifications. Region 1 exhibits a different microstructure than the fracture surface in Region 2. It was possible the sample reacted with the electrode even though it was Pt. Region 2 shows grain-necking and some interconnected porosity. It is possible this specimen did not have as high of a density as the sample in Experiment 2. However, a true evaluation of density could not be made because the specimens were too small to get precise density measurements (via pycnometry or geometric calculations).

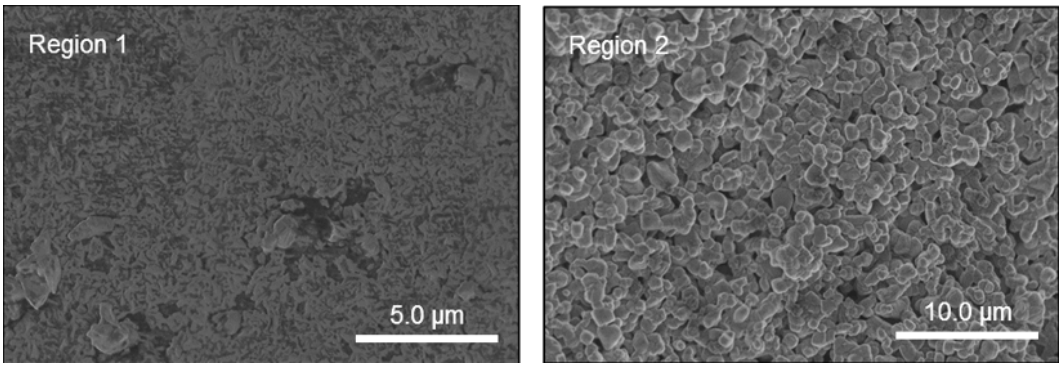

Fig. 11 SEM images of the specimen from Experiment 3 showing Region 1 (left) and Region 2 (right)

In Experiment 4, a disk with a thickness of 3.18 mm and diameter of 12.8 mm was pressed in a similar manner to the samples sintered by conventional means. The goal was to make a dense part through the thickness as a direct comparison to the conventional method. Instead, it was found that a significantly higher furnace temperature was required to observe a flash under these conditions, as shown in Fig. 12. Once the temperature of the furnace was maximized, the voltage was manually increased until the power supply switched to current control and the voltage dropped. The current was applied for 5 min after the voltage drop.

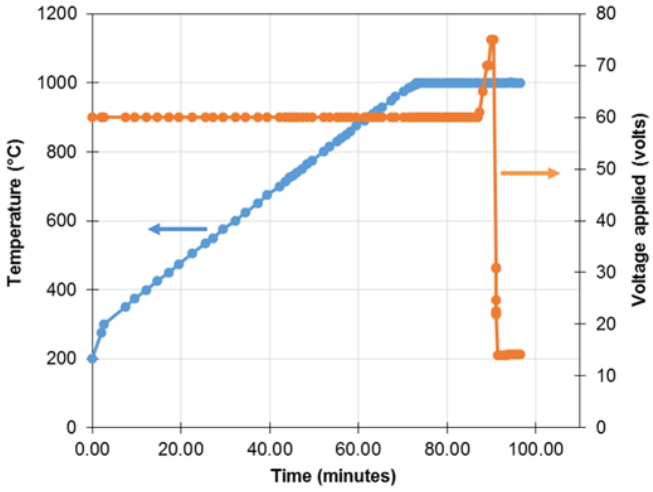

Fig. 12 Furnace temperature and applied voltage vs. time for Experiment 4; after dwelling at 1000 °C for 15 minutes, voltage was manually increased until power supply switched to current mode and the voltage dropped

Figure 13 shows an SEM image of the fracture surface from Experiment 4. The microstructure exhibits intergranular fracture with some remaining porosity. However, this SEM image was not consistent with the rest of the specimen, which

exhibited a significant amount of remnant porosity and some interesting features at the surfaces closest to the electrodes, as shown in Fig. 14.

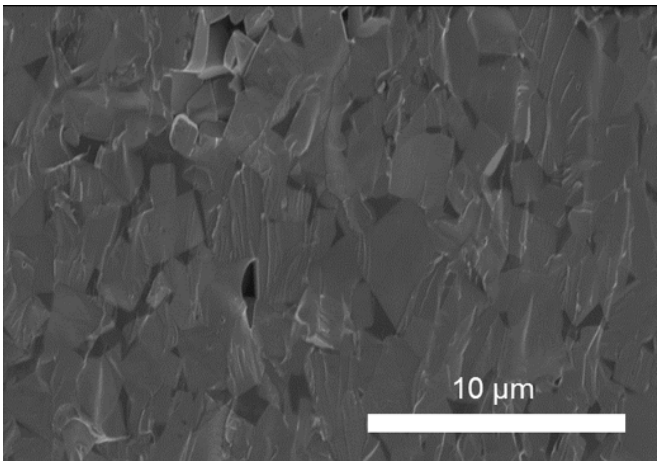

Fig. 13 SEM image of a fracture surface on the specimen from Experiment 4

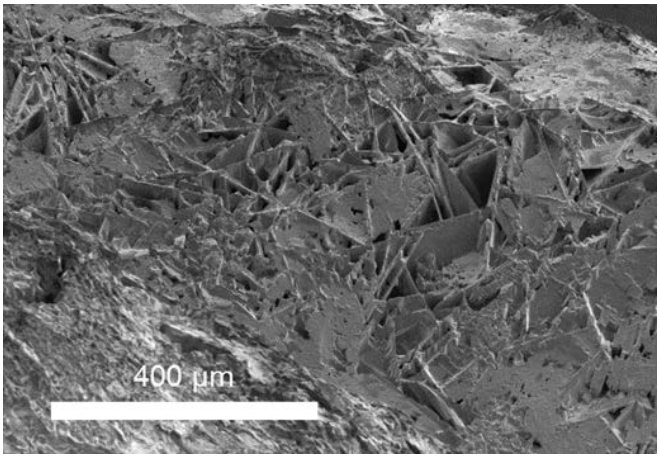

Fig. 14 SEM image of the specimen from Experiment 4 showing the area nearest the Pt electrode

3.2 Evaluation of the Phases Present

The phase content of the LLTO materials was calculated from powder-XRD data using the Rietveld method (via TOPAS). The goodness of fit (GOF) was calculated by the software, which indicated how well the calculated pattern matched the measured pattern. In TOPAS, a GOF value between 1 and 2 was considered to be an acceptable correlation. Table 2 shows the calculated phase content for the cubic and tetragonal structures. The variation between the specimens was within 10% of the mean. The data from Table 2 are depicted in Fig. 15.

Table 2 Phase content as calculated by Rietveld method from powder-XRD data along with the GOF value from TOPAS

Specimen	Tetragonal $P4/mmm$ (%)	Cubic $Pm\bar{3}m$ (%)	GOF
Starting powder	38.4	61.6	1.24
Pressureless sintered	43.7	56.3	1.28
Sintered and quenched	34.4	65.6	1.32
Experiment 2	44.3	55.7	1.33
Experiment 3	45.2	54.8	1.23
Experiment 4	56.7	43.3	1.49

It was expected the specimen with the highest percent of cubic structure was conventionally sintered and quenched in liquid nitrogen. Since all of the flash-sintered specimens had a lower percent of cubic structure than the quenched sample (from previous work), it was possible the rate of temperature change in the flash experiments was unable to preserve the cubic polymorph. The furnace temperature of Experiment 4 was a maximum of 1000 °C, which is lower than the expected cubic-to-tetragonal-transition temperature of approximately 1100 °C; hence, the greater proportion of the tetragonal phase in Experiment 4.

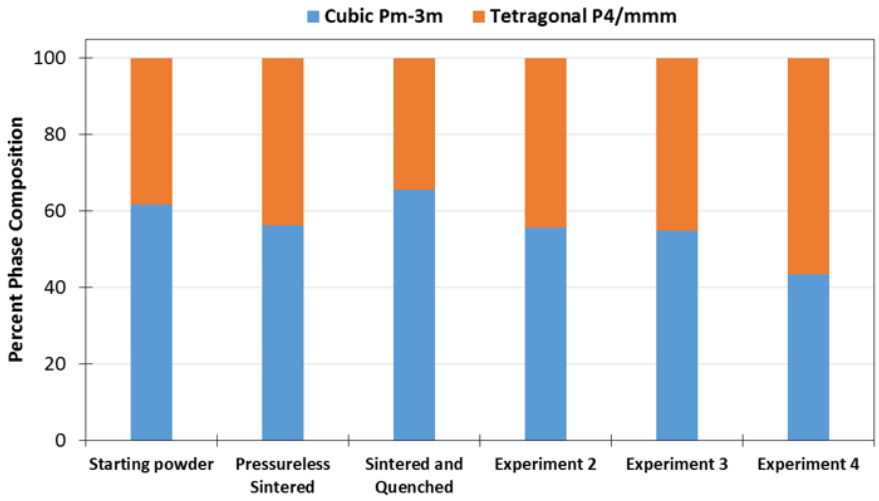

Fig. 15 Bar graph of phase content of Experiments 2–4 and the comparison specimens from previous work

3.3 Comparing the Ionic Conductivity

The flash-sintered LLTO specimens were very fragile and typically broke into small fragments over time. However, two specimens from Experiments 3 and 4 were polished down to parallelepipeds for EIS measurements. Figure 16 shows the

raw and modelled data for the specimen from Experiment 3. While the specimen exhibited stronger electronic than ionic conduction, grain and grain-boundary resistances were still calculated. Figure 17 shows the raw and modelled data for the specimen from Experiment 4.

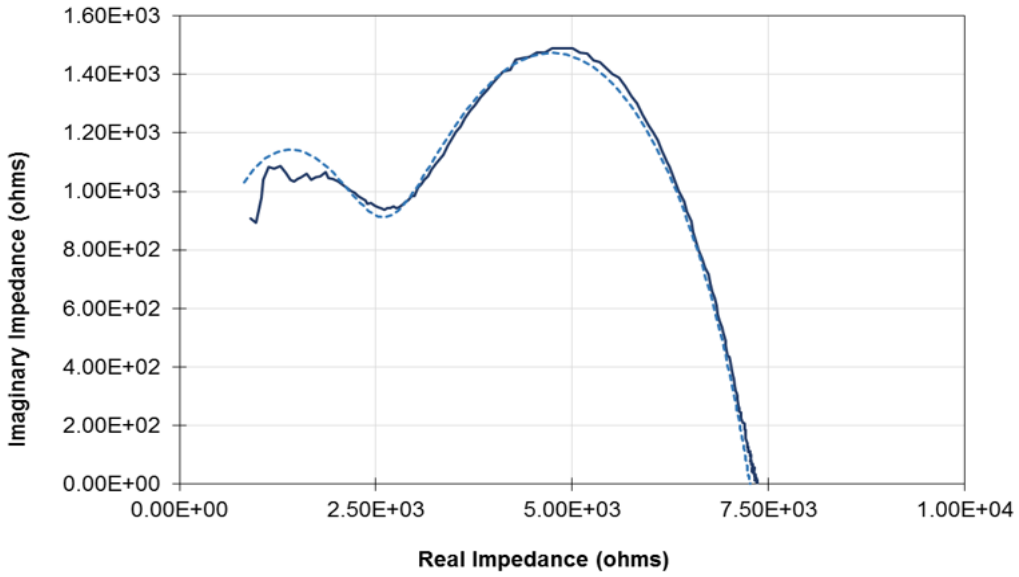

Fig. 16 Imaginary impedance vs. real impedance in ohms for the specimen from Experiment 3; solid line represents measured data and dashed line represents the model of an equivalent circuit

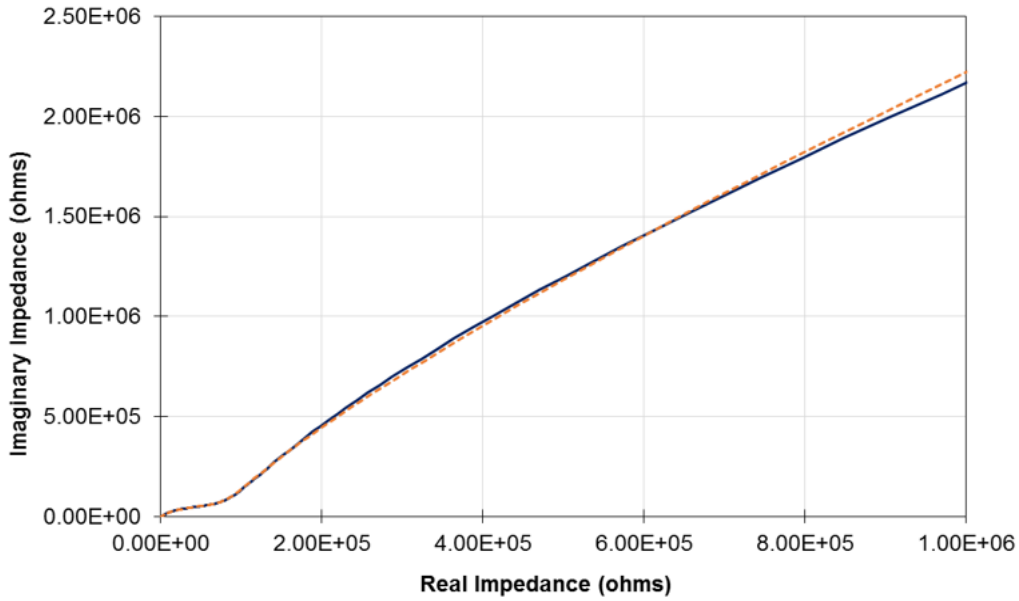

Fig. 17 Imaginary impedance vs. real impedance in ohms for the specimen from Experiment 4; solid line represents measured data and dashed line represents the model of an equivalent circuit

Figure 18 shows the calculated lattice ionic conductivity in Siemens per centimeter (S/cm). The pressureless-sintered and sintered-and-quenched samples exhibited higher lattice conductivity than the flash-sintered samples. One possible explanation was the lower percent of cubic structure resulted in a lower conductivity. Figure 19 shows the grain-boundary ionic conductivity of the specimens. Recall that the grain-boundary ionic conductivity was the limiting contribution to the total ionic conductivity of the material. The specimen from Experiment 3 had the highest grain-boundary conductivity among the measured specimens, even though the raw data appeared to be more electronically conducting (movement of electrons through the lattice). It was possible the lower temperature of the furnace reduced the amount of lithium volatilization, leading to more lithium ion charge carriers available for transport at the grain boundaries.

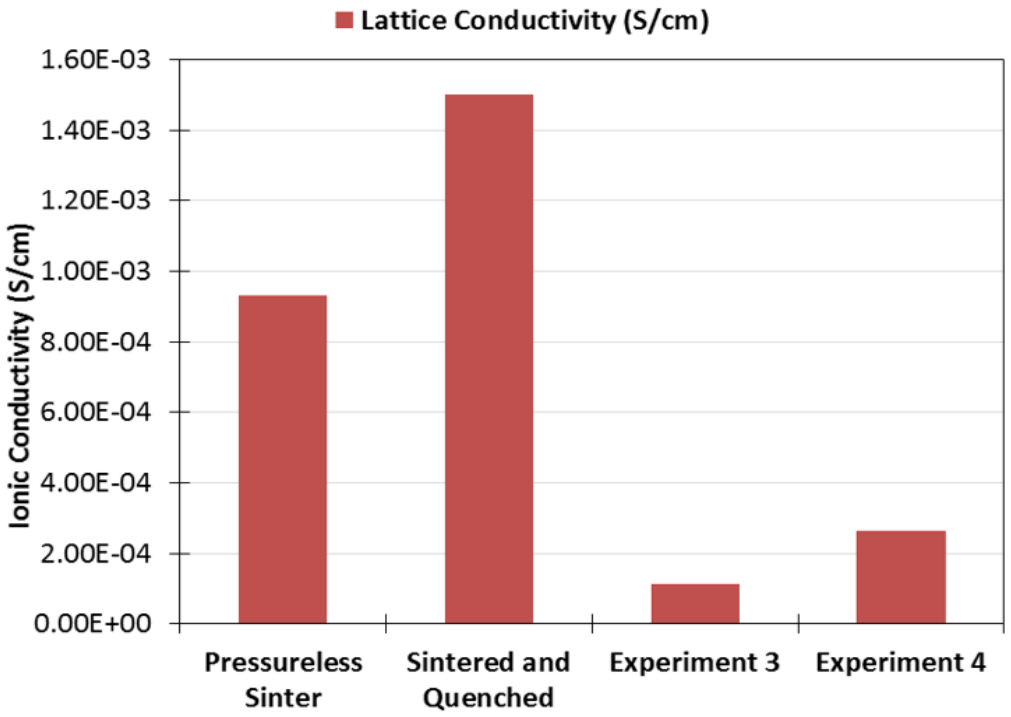

Fig. 18 Calculated ionic conductivity of the grain for four different specimens: two flash-sintered specimens (Experiments 3 and 4) compared with conventionally sintered samples

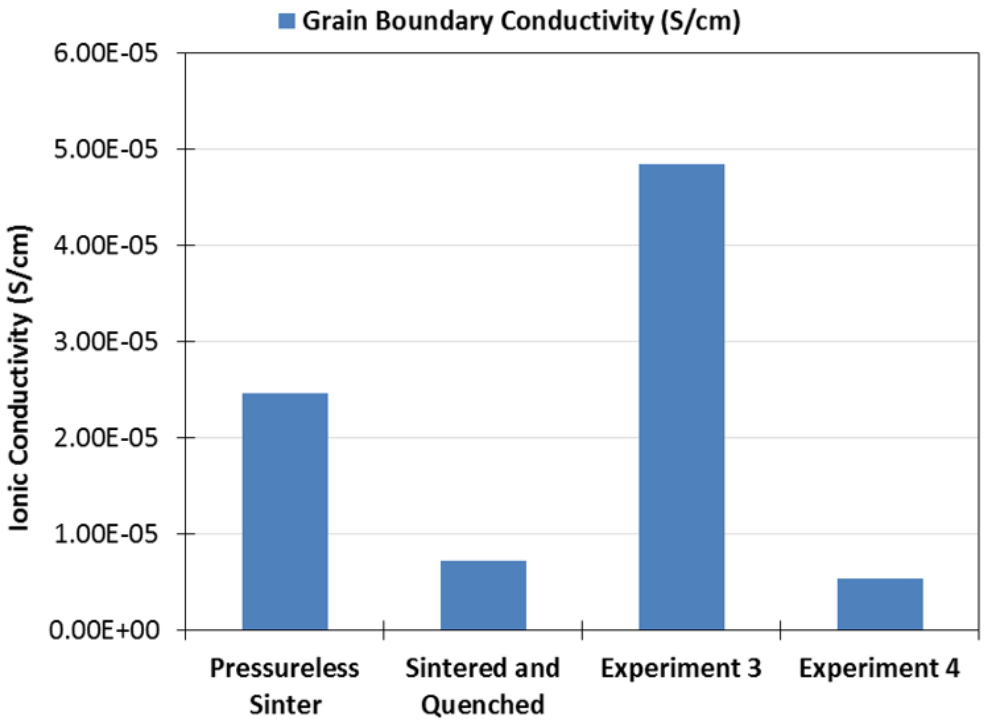

Fig. 19 Calculated grain-boundary ionic conductivity for four different specimens: two flash-sintered specimens (Experiments 3 and 4) compared with conventionally sintered samples

4. Conclusions and Ongoing Work

Four experiments were completed using a flash-sintering procedure to produce sintered LLTO specimens. Microstructural, physical, and electrical characterization were conducted on the sintered samples. The flash-sintered specimens were compared to conventionally processed materials.[8] All flash-sintered specimens exhibited the typical "flash" behavior and demonstrated varying degrees of densification. All of the samples exhibited nonuniform densification, which could have been a result of the sample size. Since all of the specimens were larger than those mentioned in the literature, it was possible that once the current pathways were formed on the outside of the specimen, the sample became conductive and densification no longer occurred. These experiments have indicated a few different processing parameters can affect the onset of the flash event, including sample size, green density, and electrode configuration. The grain-boundary conductivity from Experiment 3 was higher than the conventionally sintered control specimen but with a trade-off on the lattice conductivity.

Future efforts will focus on carefully controlling the specimen size and green density and observing changes in the flash temperature (furnace temperature at the onset of the flash event) and ionic conductivity as the applied voltage is varied. The

goal will be to consistently produce parts with uniform density. Based on the results of this study, some of the challenges will include reaction with the electrodes and potentially reducing atmospheres. Future experiments should also examine the effects of the furnace atmosphere on the composition; an oxidizing atmosphere could be beneficial to retaining the Ti^{4+} cation. Finally, significant understanding of the fundamental mechanisms could be gained by further incorporation of in-situ characterization methods.

5. References

1. Padbury R, Zhang X. Lithium–oxygen batteries—Limiting factors that affect performance. J Pow Sou. 2011;196(10):4436–4444.

2. Sutorik A, Green M, Cooper C, Wolfenstine J, Gilde G. The comparative influences of structural ordering, grain size, Li-content, and bulk density on the Li+-conductivity of Li0.29La0.57TiO3. J Mater Sci. 2012;47(19):6992–7002.

3. Stramare S, Thangadurai V, Weppner W. Lithium lanthanum titanates: a review. Chem Mater. 2013;15(21):3974–3990.

4. Kawai H, Kuwano J. Lithium ion conductivity of A-site deficient perovskite solid solution La0.67-xLi3xTiO3. J Electroch Soc. 1994;141(7):L78–L79.

5. Weiss Brennan CV, Blair VL, Marsico JM. Density optimization of lithium lanthanum titanate ceramics for lightweight lithium-air batteries. Aberdeen Proving Ground (MD): Army Research Laboratory (US); 2014 Nov. Report No.: ARL-TR-7145.

6. Ban CW, Choi GM. The effect of sintering on the grain boundary conductivity of lithium lanthanum titanates. Sol Sta Ion. 2001;140(3–4):285–292.

7. Wolfenstine J, Allen JL, Weiss Brennan CV, Blair VL. Conductivity of hot isostatically pressed Li0.35La0.55TiO3. Adelphi (MD): Army Research Laboratory (US); 2015 Aug. Report No.: ARL-TR-7401.

8. Blair VL, Weiss Brennan CV, Marsico JM. Grain boundary engineering of lithium-ion-conducting lithium lanthanum titanate for lithium-air batteries. Aberdeen Proving Ground (MD): Army Research Laboratory (US); 2016 Jan. Report No.: ARL-TR-7584.

9. Harada Y, Hirakoso Y, Kawai H, Kuwano J. Order–disorder of the A-site ions and lithium ion conductivity in the perovskite solid solution La0.67−xLi3xTiO3 (x=0.11)1. Sol Sta Ion. 1999;121(1–4):245–251.

10. Inaguma Y, Katsumata T, Itoh M, Morii Y. Crystal structure of a lithium ion-conducting perovskite La2/3−xLi3xTiO3 (x=0.05). J Sol Sta Chem. 2002;166(1):67–72.

11. Sommariva M, Catti M. Neutron diffraction study of quenched Li0.3La0.567TiO3 lithium ion conducting perovskite. Chem Mater. 2006;18(9):2411–2417.

12. Varez A, Fernández-Díaz MT, Alonso JA, Sanz J. Structure of fast ion conductors Li3xLa2/3-xTiO3 deduced from powder neutron diffraction experiments. Chem Mater. 2005;17(9):2404–2412.

13. Cologna M, Prette ALG, Raj R. Flash-sintering of cubic yttria-stabilized zirconia at 750°C for possible use in SOFC manufacturing. J Amer Ceram Soc. 2011;94(2):316–319.

14. Raj R. Joule heating during flash-sintering. J Euro Ceram Soc. 2012;32(10):2293–2301.

15. Candelario VM, Moreno R, Todd RI, Ortiz AL. Liquid-phase assisted flash sintering of SiC from powder mixtures prepared by aqueous colloidal processing. J Euro Ceram Soc. 2017;37(2):485–498.

16. Ji W, Parker B, Falco S, Zhang JY, Fu ZY, Todd RI. Ultra-fast firing: effect of heating rate on sintering of 3YSZ, with and without an electric field. J Euro Ceram Soc. 2017;37(6):2547–2551.

17. Schmerbauch C, Gonzalez-Julian J, Röder R, Ronning C, Guillon O. Flash sintering of nanocrystalline zinc oxide and its influence on microstructure and defect formation. J Amer Ceram Soc. 2014;97(6):1728–1735.

18. Todd RI, Zapata-Solvas E, Bonilla RS, Sneddon T, Wilshaw PR. Electrical characteristics of flash sintering: thermal runaway of joule heating. J Euro Ceram Soc. 2015;35(6):1865–1877.

19. Zapata-Solvas E, Bonilla S, Wilshaw PR, Todd RI. Preliminary investigation of flash sintering of SiC. J Euro Ceram Soc. 2013;33(13–14):2811–2816.

List of Symbols, Abbreviations, and Acronyms

σ_b	conductivity of the bulk boundaries
σ_{gb}	conductivity of the grain boundaries
A	cross-sectional area of the specimen
Ar	argon
ARL	US Army Research Laboratory
DC	direct current
EIS	electrochemical impedance spectroscopy
GOF	goodness of fit
HIP	hot isostatic pressing
l	specimen length
Li	lithium
LLTO	$Li_{0.33}La_{0.55}TiO_3$
O_2	oxygen
Pt	platinum
R_b	bulk resistance
R_{gb}	grain-boundary resistance
SEM	scanning electron microscope
TD	theoretical density
T_f	flash temperature
T_m	melting temperature
W	tungsten
XRD	X-ray diffraction
YSZ	yttria stabilized zirconia

1 DEFENSE TECHNICAL
(PDF) INFORMATION CTR
DTIC OCA

2 DIR ARL
(PDF) IMAL HRA
RECORDS MGMT
RDRL DCL
TECH LIB

1 GOVT PRINTG OFC
(PDF) A MALHOTRA

9 ARL
(PDF) RDRL WM
J ZABINSKI
RDRL WMM
M VANLANDINGHAM
RDRL WMM E
V BLAIR
S SILTON
RDRL WMM E
R BRENNAN
L VARGAS GONZALEZ
RDRL SED C
J WOLFENSTINE
C LUNDGREN
RDRL SED
E SHAFFER